Chapter 5

Interferometry and its Applications in Surface Metrology

Dahi Ghareab Abdelsalam and Baoli Yao

Additional information is available at the end of the chapter

http://dx.doi.org/10.5772/66275

Abstract

Interferometry has been a time-honored technique for surface topography measurement. Interferometric measurements of surface shape are relative measurement techniques in which the shape of a known surface is compared with that of an unknown surface, and the difference is displayed as a series of interference fringes. Noise attached in the interference fringes can have catastrophic effects on the phase-unwrapping process, so denoising is essential before reconstruction. Some noise may be generated due to vibrations when multiple images over a finite time period are captured for reconstruction by phase-shifting technique. This harmful noise is drastically reduced when fast phase shifting–based single-shot parallel four-step combined with Fizeau interferometer is applied. Measuring the shape of strongly curved surfaces using two-beam interferometry is very complicated due to the higher fringe density. This problem may be solved by multiple-beam interferometry, thanks to the very sharp interference fringes. The experimental results show the feasibility and high precision of multiple-beam interferometry.

Keywords: interferometry, surface topography, optical aberrations, phase shifting, phase unwrapping

1. Introduction

Calibration of surfaces by optical instruments such as interferometers is a necessary step in many applications in engineering and science. The merit of using optical instruments over stylus instruments is that the optical instruments do not physically contact the surface under test and hence protect the surface from damage. In recent years, automatically controlled interferometers were engineered and provided with computer-aided technologies. A combination of moving parts controlled by various computer techniques and sophisticated electronics, and wave front fitting techniques were used to ensure precision and reliability.

However, all two-beam interferometers suffer from the fact that they produce $\cos^2$ intensity distributions. This fact makes two-beam interferometers unpopular to characterize strongly curved surfaces and steep edges because of the too high density of fringes which makes the feature too complex to measure. Multiple-beam interferometers are used to characterize these surfaces successfully thanks to the very sharp fringes. In this chapter, we present new frontiers in both two- and multiple-beam interferometers carried out by the author. As modern interferometers use a laser as the light source, spurious and speckle noises arise in the fringe pattern. Numerical techniques should be applied to the fringe pattern to suppress these spurious and speckle noises. In Section 2, limitations of optical instruments including optical aberrations and denoising and effect of noise on phase unwrapping are explained. In Section 3, fundamentals of interferometry with focus on two- and multiple-beam interferometers and their capabilities in testing film thickness, curvatures of strongly curved surfaces, and parallelism of a standard optical flat are described. It is worth mentioning that the in-line configuration of interferometry can feature finer sample spatial details compared with the off-axis configuration. However, using in-line configuration requires the time-sequent phase-shifting (PS) process to eliminate both zero-order and the twin image. Single-shot parallel phase-shifting technique is proposed for real-time measurement. In Section 4, single-shot parallel four-step phase-shifting Fizeau interferometer for three-dimensional (3-D) surface micro-topography measurement is explained. Section 5 gives concluding discussions and remarks.

2. Limitations of optical instruments

This section briefly discusses some of the limitations of optical instruments. Many optical instruments use a microscope objective to magnify the features on the surface under test. There are two fundamental limitations of the optical instruments utilizing a microscope objective: the first is the numerical aperture (Na) of the object which is given by

$$\mathrm{Na} = n\sin(\alpha) \tag{1}$$

where n is the refractive index of the medium between the objective and the surface and α is the acceptance angle of the aperture as shown in **Figure 1**. For optical instruments based on interference microscopy, a correction factor should be added to the interference pattern due to the impact of the Na. This correction can usually be estimated by well-known methods [1]. The second limitation is the optical resolution of the objective. The resolution determines the minimum distance between two lateral features on a surface that can be measured. The spatial resolution s is approximately given by

$$s = \lambda / 2\mathrm{Na} \tag{2}$$

where λ is the wavelength of the incident radiation [2]. For a theoretically perfect optical system with a filled objective pupil, the optical resolution is given by the Rayleigh criterion, where the

http://dx.doi.org/10.5772/66275

1/2 in Eq. (2) is replaced by 0.61. If the objective is not optically perfect (i.e., aberration-free) or if a part of the beam is blocked (e.g., in a Mirau interference objective, or when a steep edge is measured), the value becomes higher (worse).

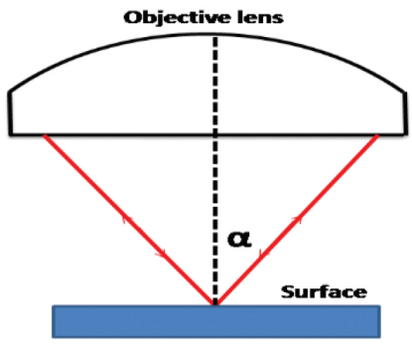

Figure 1. Numerical aperture of a microscope objective lens.

2.1. Optical aberrations

A system with aberrations has a wavefront phase surface that deviates from the ideal spherical wave. Aberrations are found in most practical imaging systems, and their effect reduces image quality. Aberrated systems tend to cause space-variant imaging, where the impulse response is not the same for each image point. **Figure 2** shows the representation of an ideal spherical and aberrated wavefronts. The difference between the ideal spherical wavefront and aberrated wavefront is a wavefront error $W(x,y)$, where x and y are the coordinates in the pupil plane. It is worth noting that the source of aberrated wavefronts may come from the imperfections in the imaging optics.

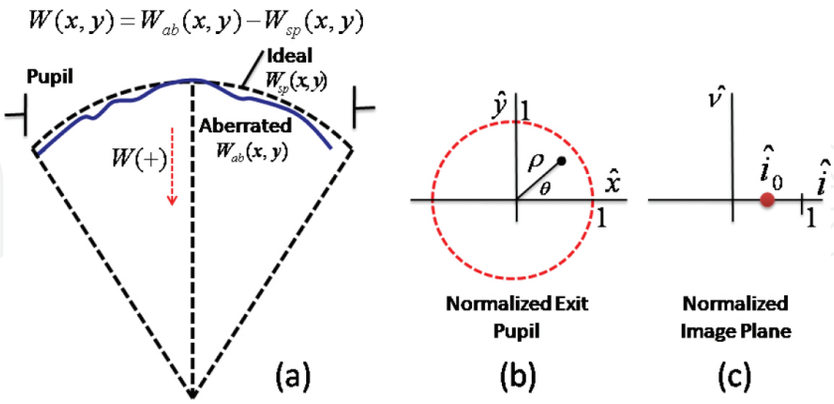

Figure 2. (a) Spherical (sp) and aberrated (ab) wavefronts, (b) Seidel aberration coordinate definitions for the normalized exit pupil, and (c) Seidel aberration coordinate for the normalized image plane.

Wavefront optical path length (OPD) is commonly described by a polynomial series. The Seidel series is used by optical designers because the terms have straightforward mathematical relationships to factors such as lens type and position in the image plane. Another series,

Zernike polynomials, is used in optical testing and applications where the aberrations do not have a simple dependency on the system parameters. Both formulations assume a circular pupil. Seidel polynomials are often used to describe monochromatic aberrations for rotationally symmetric optical systems, such as most lenses and mirrors. A common form that is applied in conventional imaging systems is described by [3]

$$W(\hat{i}_0;\rho,\theta)=\sum_{j,m,n} W_{klm}\hat{i}_0^{\,k}\rho^l\cos^m\theta;\; k=2j+m,\quad l=2n+m, \tag{3}$$

where ρ is a normalized radial distance in the exit pupil and θ is the angle in the exit pupil as shown in **Figure 2(b)**. For computational reasons, the angle θ is defined here relative to the x-axis in a counter-clockwise direction. However, note that this angle is often defined relative to the y-axis in traditional aberration treatments. The normalized exit pupil has a radius of 1 where the physical coordinates (x, y) are divided by the exit pupil radius to get normalized coordinates $(\hat{x},\hat{y})$. $\hat{i}_0$ is the normalized image height, defined along the $\hat{i}$ axis in the imaging plane as indicated in **Figure 2(c)**. The normalized image height is the physical height of a given point in the image divided by the maximum image radius being considered. Since the Seidel polynomials assume a rotationally symmetric system, the pupil and image plane coordinate systems are simply rotated to find the wavefront OPD function for an image point that is off the $\hat{i}$ axis. The indices j, m, n, and so forth, in Eq. (3), are a numbering and power scheme. W_{klm} are the wavefront aberration coefficients, and the five primary Seidel aberrations correspond to $k+l=4$. These primary aberrations are known as spherical aberration, coma, astigmatism, field curvature, and distortion. The coefficients have units of distance (μm), although they are usually discussed relative to the optical wavelength (i.e., so many "waves").

For simulation purposes, it is convenient to convert from polar to Cartesian coordinates. Referring to **Figure 2(b)**,

$$\rho=\sqrt{\hat{x}^2+\hat{y}^2}\quad\text{and}\quad\rho\cos\theta=\hat{x}, \tag{4}$$

and the primary aberrations are then written as

$$\begin{aligned}W(\hat{i}_0;\hat{x},\hat{y}) &= W_d(\hat{x}^2+\hat{y}^2)+W_{040}(\hat{x}^2+\hat{y}^2)^2+W_{131}\hat{i}_0(\hat{x}^2+\hat{y}^2)\hat{x}\\ &\quad+W_{222}\hat{i}_0^{\,2}\hat{x}^2+W_{220}\hat{i}_0^{\,2}(\hat{x}^2+\hat{y}^2)+W_{311}\hat{i}_0^{\,3}\hat{x}.\end{aligned} \tag{5}$$

The first term in this series is not one of the five primary aberrations, but is a defocus term. It is the wavefront OPD that is "created" in moving the image plane along the optical axis from the paraxial focus position. The second, third, fourth, and fifth Seidel aberration terms in Eq. (5) are spherical, coma, astigmatism, field curvature, and distortion, respectively. Simulating the effects of these aberrations by plotting some wavefront OPD surfaces is shown

in **Figure 3**. **Figure 3** illustrates that spherical aberration (*W*040) and field curvature (*W*220) are wavefront curvature-like terms that are spherically symmetric with respect to the pupil coordinates. Coma (*W*131) and astigmatism (*W*222) are not spherically symmetric and depend on the image point position.

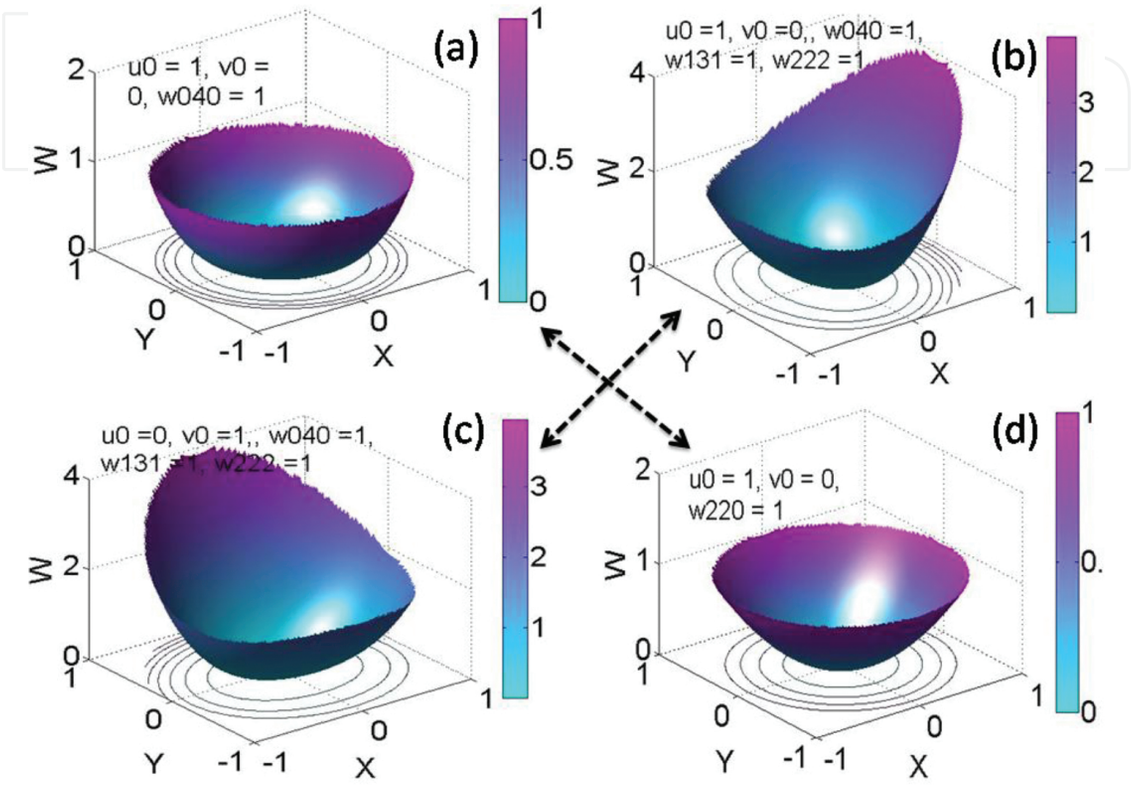

Figure 3. Example wavefront OPD surface and contour plot using Seidel 5. These represent phase surfaces that are applied in the exit pupil.

Because of the great coherence of the laser light, the fringe pattern may be easily obtained. This advantage of laser light makes most of the modern interferometers use a laser as the light source. In fact, this advantage can also be a serious disadvantage, as spurious and speckle noises arise. Special precautions must be taken into account to suppress these spurious and speckle noises. Some of them are practical such as inserting many stops in the optical system and the others are numerical such as applying windowed Fourier transform (WFT) [4] and flat fielding with apodization techniques [5].

2.2. Denoising and effect of noise on phase unwrapping

When an optically rough surface is illuminated by an expanded laser beam, the formed image is a speckle pattern (bright and dark spots). Noise can have catastrophic effects on the phase-unwrapping process. Application of simple filtering techniques in classical image processing to suppress speckle noise tends to do more harm than good, because they blur the image indiscriminately. Alternative techniques must be applied to obtain a clean interference pattern.

Once a clean image is obtained, unwrapping process is applied easily for reconstruction. Let us see how the noise affects on phase unwrapping, suppose that we have a discrete signal whose amplitude exceeds the range $[-\pi,\pi]$ as shown in **Figure 4(a)**. We can wrap the signal $x(n)$ by calculating the sinusoidal and the cosinusoidal values of $x(n)$. The four quadrant arctangent function (atan2) of $\sin(x)$ and $\cos(x)$ is then calculated using the following equation:

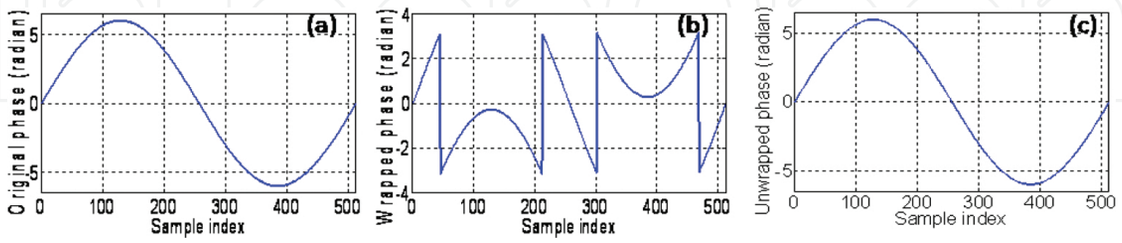

Figure 4. (a) Continuous phase, (b) wrapped phase, and (c) the phase unwrapped signal.

$$a\tan 2(u,v) = \begin{cases} \tan^{-1}(u/v) & 1st.\ quadrant \\ \tan^{-1}(u/v)+\pi & 2nd.\ quadrant \\ \tan^{-1}(u/v)-\pi & 3rd.\ quadrant \\ \tan^{-1}(u/v) & 4th.\ quadrant \end{cases} \tag{6}$$

where u and v are real numbers. We can express the wrapping process mathematically as $x_w(n) = w[x(n)]$. The 2π jumps that are present in the wrapped phase signal that is shown in **Figure 4(b)** must be removed in order to return the phase signal $x_w(n)$ to a continuous form and hence make the phase usable in any analysis or further processing. This process is called phase unwrapping and has the effect of returning a wrapped phase signal to a continuous phase signal that is free from 2π jumps. We can express the unwrapping process mathematically as $x_U(n) = x_w(n) + 2\pi k$, where $x_U(n)$ is the unwrapped phase signal and k is an integer.

The phase-unwrapped signal is shown in **Figure 4(c)**. The wrapped phase signal that is shown in **Figure 4(a)** is a very simple signal to unwrap. This is because $x_w(n)$ is a simulated signal that does not contain any noise, but if the signal is noisy, a fake-phase wrap may be produced by noise in the signal. The existence of a fake wrap will affect the unwrapping of the sample. Let us use a computer simulation to illustrate this. Suppose that we have the discrete signal $x_w(n)$ and then we add white noise to this signal as $x_{\text{noise}}(n) = x(n) + \text{white noise}$. The noise variance is set to a higher value of 0.8. The original noisy signal is shown in **Figure 5(a)**. Wrapping and unwrapping phase signals are shown in **Figure 5(b)** and **(c)**, respectively. As shown in **Figure 5**, the higher noise level has seriously affected the phase-unwrapping process and the phase unwrapping of the signal became a challenging task. This is due to the existence of a fake wrap in the signal.

http://dx.doi.org/10.5772/66275

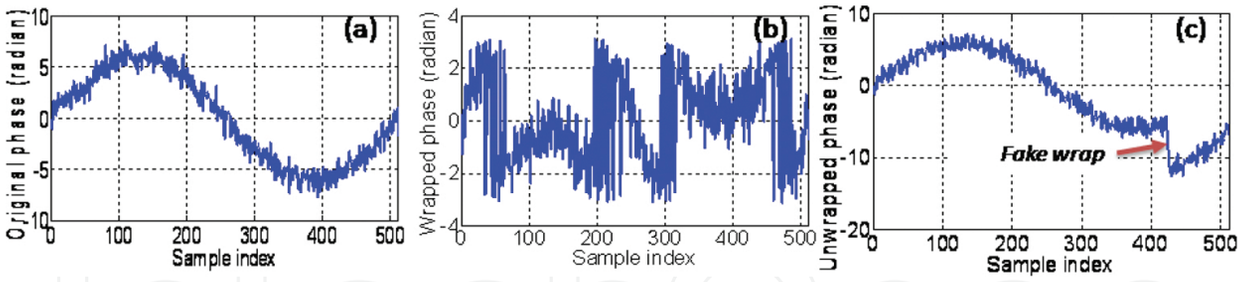

Figure 5. (a) Original noisy signal, (b) the phase wrapped signal, and (c) the phase unwrapped signal. Here, the noise variance has been increased to a value of 0.8.

Some techniques such as windowed Fourier transform and flat fielding with apodization may be used to suppress the noise and solve the problem of fake wrap. **Figure 6(a)** shows a simulated noisy closed fringe, and a clean image is shown in **Figure 7(b)** obtained using WFT technique. Profiles at the middle of **Figure 6(a)** and **(b)** are shown in **Figure 6(c)**. **Figure 7(a)** shows an experimental inline interferogram of a nano-pattern taken by Mach-Zehnder interferometer and a clean image is shown in **Figure 7(b)** obtained using flat fielding with apodization technique. Profiles at the middle of **Figure 7(a)** and **(b)** are shown in **Figure 7(c)** up and down, respectively.

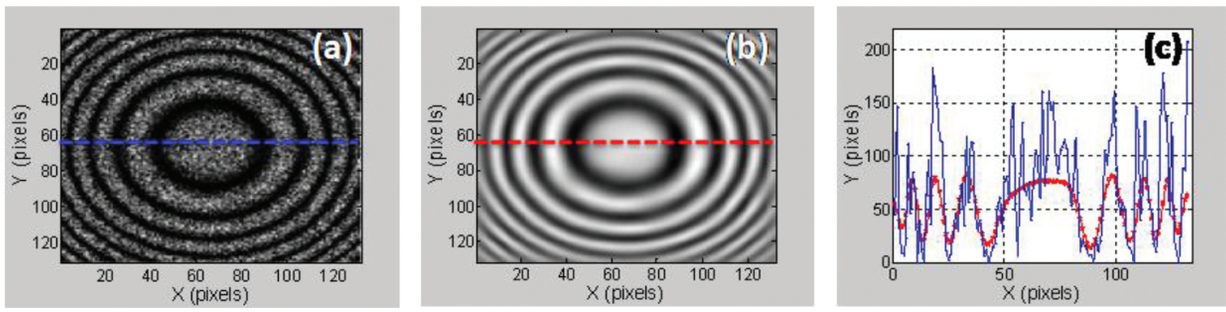

Figure 6. A simulated noisy closed fringes (a), a clean image of **Figure 7(a)** obtained using WFT technique (b), and profiles at the middle of **Figure 7(a)** and **(b) (c)**.

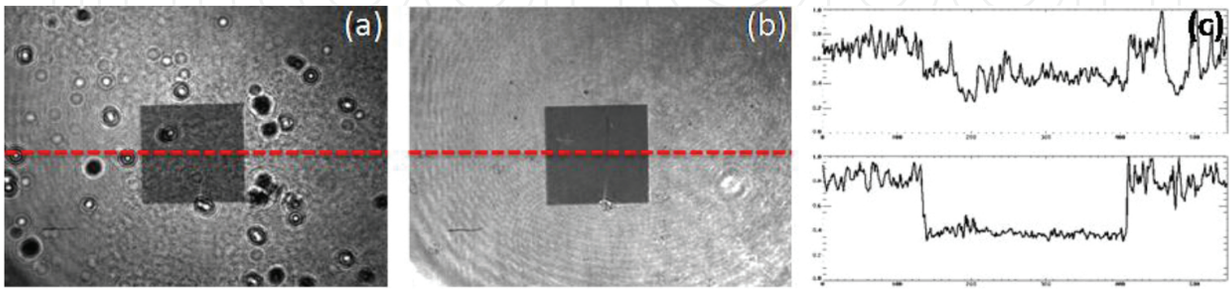

Figure 7. An empirical inline interferogram of a nano-pattern object (a), a clean image of **Figure 7(a)** obtained using flat fielding with apodization technique (b), and profiles at the middle of **Figure 7(a)** and **(b)**, up and down, respectively, (c).

Several basic interferometric configurations are used in optical-testing procedures, but almost all of them are two-beam interferometers. In Section 3, we review fundamentals of interferometry with focus on two- and multiple-beam interferometers and its capability in featuring the topography of surfaces.

3. Fundamentals of interferometry

Interferometry is the technique of superposing two or more waves, to create an output wave that differs from the input waves [6]. An interferometer is an optical instrument that can measure small wavefront deformations with a high accuracy, of the order of a fraction of the wavelength. Two-beam interferometers produce an interferogram by superimposing two wavefronts, one of which is typically a flat reference wavefront and the other a distorted wavefront from the object, whose shape is to be measured. To study the main principles of interferometers, let us consider from Maxwell's equations that the electric field of a plane wave, with speed, c, frequency, f, and wavelength, λ, travelling in the z-direction, is given by

$$E(z,t) = \begin{pmatrix} E_x \\ E_y \end{pmatrix} e^{i(kz-\omega t)} \tag{7}$$

where $\omega = 2\pi f = 2\pi c/\lambda$ is the circular frequency and $k = 2\pi/\lambda$ is the circular wave number. Assume that $E_y = 0$, that is, the light is linearly polarized in the x-direction. At the location $z = 0$, the electric field $E = E_x \cos\omega t$. The intensity is given by the square of the amplitude, thus

$$E(z) = \langle E.E \rangle = (E_x^2)\langle \cos^2 \omega t \rangle. \tag{8}$$

Consider a two-wave interferogram with flat wavefronts $E_1(t)$ and $E_2(t)$ reflected from the two mirrors of Michelson interferometer and combined at the detector. According to the principle of superposition, we can write

$$E(t) = E_1(t) + E_2(t). \tag{9}$$

Combining Eqs. (7)–(9), with some additional assumptions, gives finally

$$I = I_1 + I_2 + 2\sqrt{I_1 I_2}\cos\left(\frac{4\pi\Delta L}{\lambda}\right) \tag{10}$$

Eq. (10) is the essential equation of interference. Depending on the term $4\pi\Delta L/\lambda$, the resultant intensity on a detector can have a minimum or a maximum, and it depends on the path

http://dx.doi.org/10.5772/66275

difference or the wavelength. It is evident from Eq. (10) that the intensity has maxima for $4\pi\Delta L/\lambda = 2p\pi$, with $p = 0, \pm 1, \pm 2, \ldots$, so that $\Delta L = p\lambda/2$ and minima for $\Delta L = (p + 0.5)\lambda/2$. If the intensities I_1 and I_2 are equal, Eq. (10) reduces to

$$I = 2I_1\left(1 + \cos\left(\frac{4\pi\Delta L}{\lambda}\right)\right) = 4I_1\cos\left(\frac{2\pi\Delta L}{\lambda}\right). \tag{11}$$

This means that the minimum intensity is zero and the maximum intensity is $4I_1$. Also, it is clear that if I_1 or I_2 are zero, the interference term vanishes and a constant intensity remains. The relative visibility, V, of the interference can be defined as

$$V = \frac{I_{\max} - I_{\min}}{I_{\max} + I_{\min}} = \frac{2\sqrt{I_1 I_2}}{I_1 + I_2}. \tag{12}$$

If the magnitude of the optical path length between the two beams is greater than the temporal coherence length of the light source of the two beams, fringes will not be observed. As the OPD returns to zero, fringe visibility reaches a maximum. Temporal coherence $L_c = \lambda_c^2/\Delta\lambda$ is inversely proportional to the spectral bandwidth of the light source of the two beams, where λ_c is the center wavelength and $\Delta\lambda$ is the spectral bandwidth, measured at the full-width half maximum (FWHM) at short coherent length. It is worth mentioning that temporal coherence goes as the Fourier transform of the spectral distribution of the source. **Figure 8** shows two types of temporal coherence length: the left side is the long coherent length emitted from a laser source (spectral bandwidth very small). The Fourier transform of a zero bandwidth source is a constant, so the temporal coherence is infinite. The right side is the short coherent length emitted from a femtosecond laser with FWHM around 30 μm.

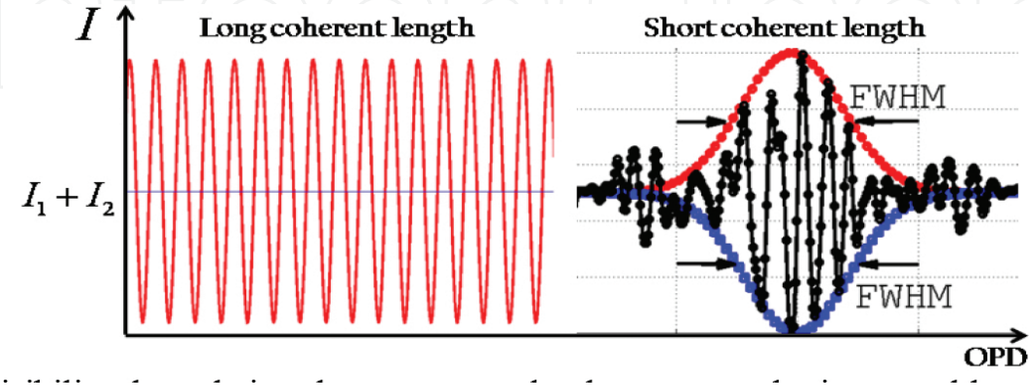

Figure 8. Fringe visibility degradation due to temporal coherence can be improved by varying the OPD between the two beams.

3.1. Two-beam interferometry

It has been noted that measuring the feature height of asphere surfaces and strongly curved surfaces using two-beam interferometers is very complicated due to the higher fringe density [7], so it has been shown that it is possible to measure the asphere form using multiple beam fringes. This is because two-beam interferometers suffer from the fact that they produce $\cos^2$ intensity distributions. **Figure 9(a)** and **(b)** compare precontour fringes of asphere surface obtained by two-beam Fizeau interferometry and multiple-beam Fizeau interferometry, respectively. As seen from **Figure 9(b)**, the multiple-beam Fizeau interferometry has the ability to resolve very small irregularities compared to common two-beam Fizeau interferometry. In this chapter, we review some of two- and multiple-beam interferometers for surface micro-topography measurement.

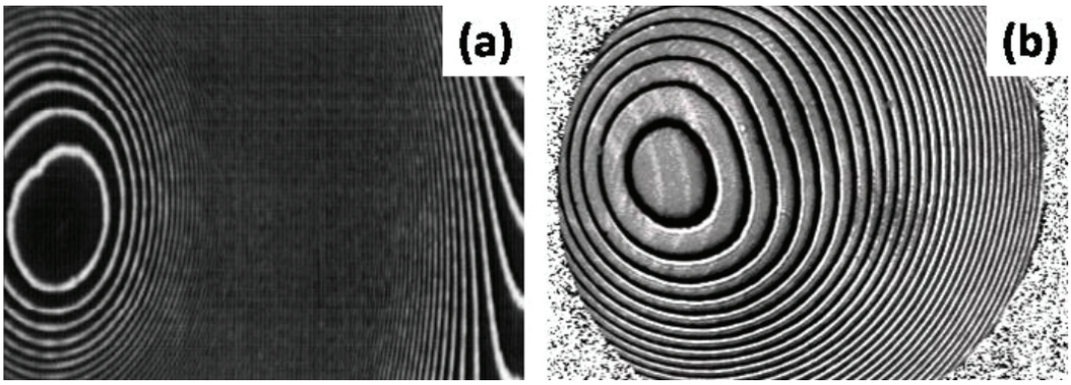

Figure 9. Precontour fringes of asphere surface obtained by (a) two-beam Fizeau interferometry and (b) multiple-beam Fizeau interferometry.

3.1.1. Twyman-Green interferometer

The light source used in a Twyman-Green interferometer is a quasi-monochromatic point source that is collimated by a collimating lens. This collimated light is incident on a beamsplitter which divides the beam into two copies: a reference beam and a test beam. The interferometer is used here for testing a spherical optical flat. The reference beam is incident on the known reference optical flat and returns to the beamsplitter. The test beam is incident on the unknown test part and also returns to the beamsplitter. The beams from the reference and the object interfere at the beamsplitter and constitute an interferogram relayed by an imaging lens to the observation plane. **Figure 10** shows a Twyman-Green interferometer for testing a curved surface in reflection [8, 9]. The reference is an optical flat of 1 inch in size and flatness of $\lambda/20$ nm. The object being tested is a curved surface of radius of curvature around. The sample is mounted carefully and four inline interferograms (no tilt between the reference and the object) are captured with phase shift between images of $\pi/2$ as shown in **Figure 11**. The intensities in the four fringe patterns can be expressed as follows:

http://dx.doi.org/10.5772/66275

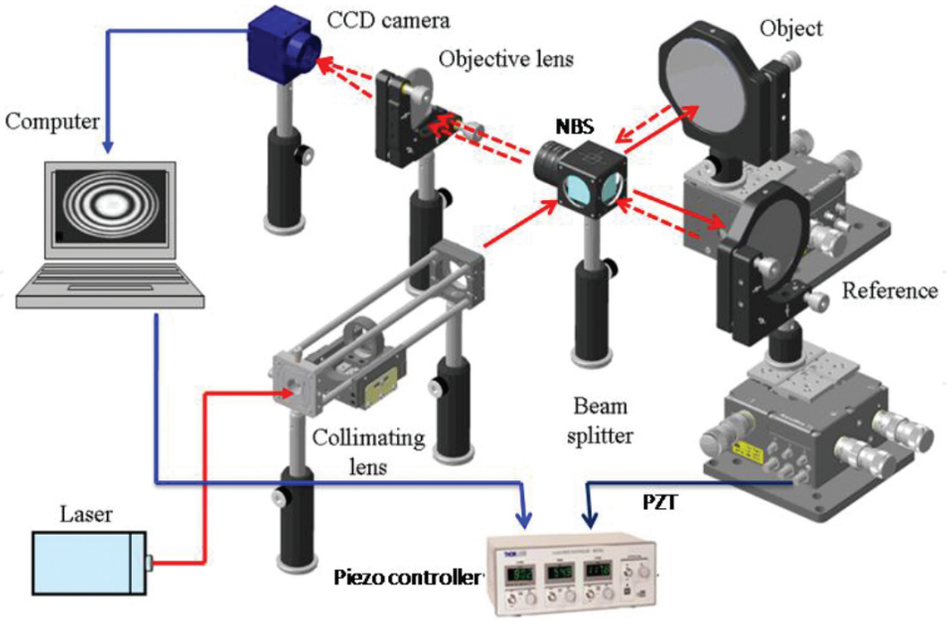

Figure 10. Optical schematic of the Twyman-Green interferometer.

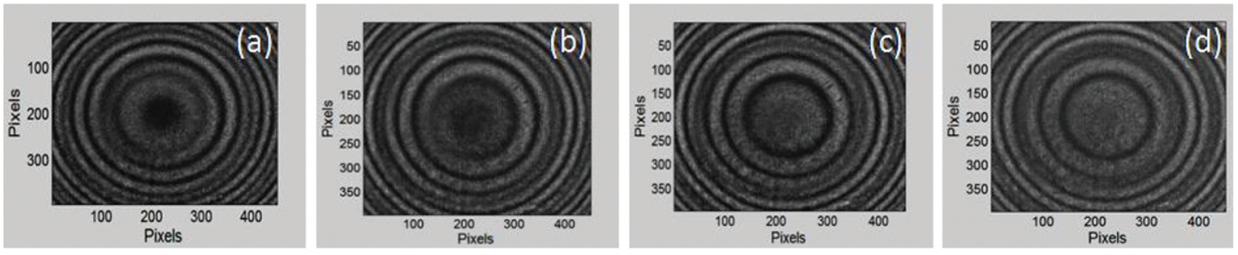

Figure 11. Intensity images of a curved object with a phase shift of 0π, 0.5π, 1π, and 1.5π, for (a–d), respectively.

$$I_j(x,y) = I_O + I_R + 2\sqrt{I_O I_R}\cos(\varphi + (j-1)\pi/2), \tag{13}$$

where I_O and I_R are the intensities of the object and the reference waves, respectively, φ is the phase encoded in the intensity distribution, and $j = 1, 2, 3$ and 4 (four frames) is the number of the phase-shifted frames.

Using the four-phase step algorithm, the phase distribution φ can be expressed as follows:

$$\varphi = \tan^{-1}\left(\frac{(I_4 - I_2)}{(I_1 - I_3)}\right). \tag{14}$$

The evaluated phase is wrapped between $-\pi$ and π due to arctangent function. The wrapped phase map resulted from the four frames in **Figure 11** is shown in **Figure 12(a)**.

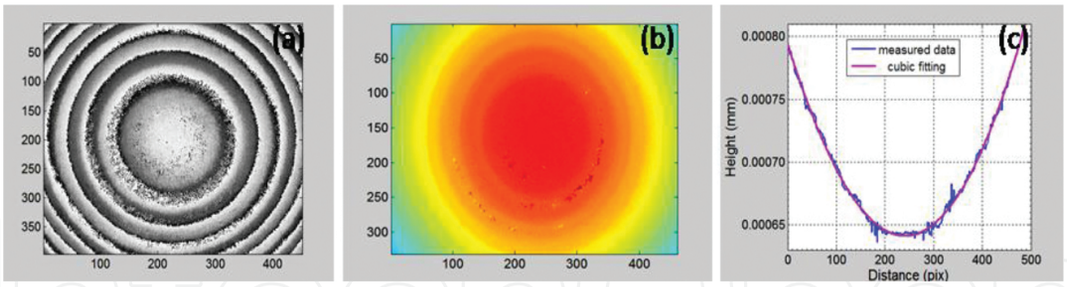

Figure 12. (a) Wrapped phase map resulted from the four frames of **Figure 10**; (b) 3-D unwrapped phase map of (a); and (c) two-dimensional height at the middle of (b) in the x-direction.

The wrapped phase map is then unwrapped to remove the 2π ambiguity and the unwrapped phase map is shown in **Figure 12(b)** and profile along **Figure 12(b)** is shown in **Figure 12(c)**.

3.1.2. Fizeau interferometers

Fizeau interferometers are most commonly used for testing surface figure, flatness, and parallelism of optical components. **Figure 13** shows a schematic diagram of a commercial laser phase-shifting Fizeau interferometer equipped with a tunable laser. Two-beam Zygo interferometer of type VeriFireMST and wavelength 632.467 nm at PTB, Germany, was used to measure the flatness of a high-flatness optical flat of size 60 mm (photograph of the optical flat being tested is shown in **Figure 13**). The reference of the interferometer is a transmission optical flat of 100 mm in size and flatness of $\lambda/500$ nm. Zygo's advanced phase analysis methods are coupled with fast Fourier transformation to separate each of these individual frequencies [10]. When the optical flat is carefully positioned on the interferometer, four different frequency patterns are obtained due to reflections from the surfaces as shown in the schematic diagram in **Figure 13**. The reflections are from the transmission flat (S_1), plate front surface (S_2), plate back surface (S_3), and reference surface (S_4).

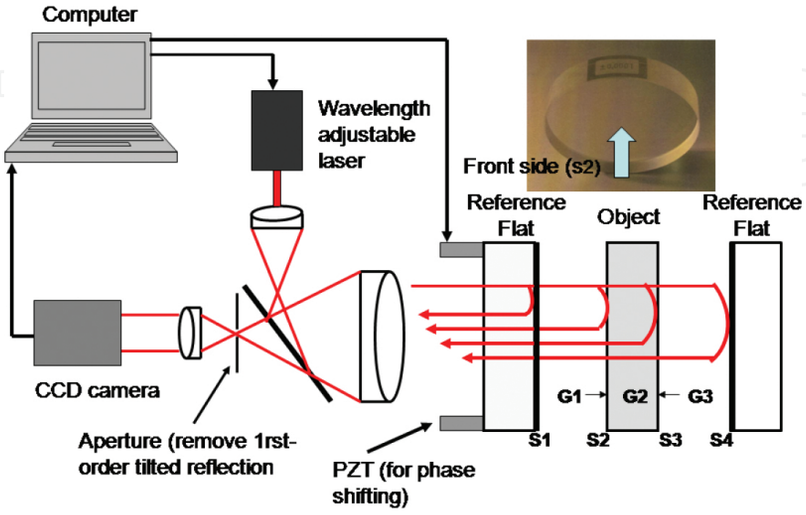

Figure 13. Familiar transmitted wavefront test geometry using a commercial laser Fizeau interferometer.

http://dx.doi.org/10.5772/66275

Because the object (optical flat) is relatively thin (G_2 = 15 mm), the gap G_1 is the intermediate thickness of 100 mm, and G_3 the thickest (115 mm) as shown from the three peaks of the OPD spectrum plot in **Figure 14(a)**. Each peak in the spectrum corresponds to the OPL of a particular elemental cavity. The spatial phase variation for the interferometer cavity is calculated according to the OPL. The interferogram in a four-surface cavity is shown in **Figure 14(b)**. The horizontal fringes correspond to the interference of the front side S_2 of the optical flat and the reference, while the second inclined dark fringes correspond to the interference of the back surface of the object S_3 and the reference. The software analyzes each fringe pattern and the surface from of the optical flat was obtained. **Figure 14(c)** shows the phase map of the front side of the sample, and profiles through x- and y-directions are shown in **Figure 15**, respectively. The measurement has been calculated at a temperature of 20.5°C with uncertainty in the measurement of 15 nm.

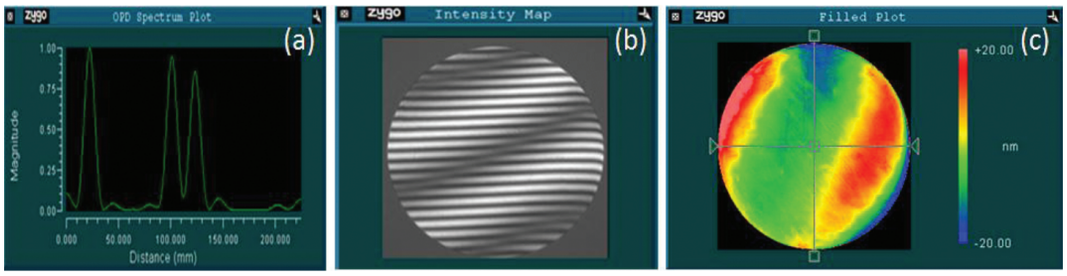

Figure 14. (a) Peaks of the OPD spectrum; (b) interferogram in a four-surface cavity; and (c) phase map of the front side of the sample.

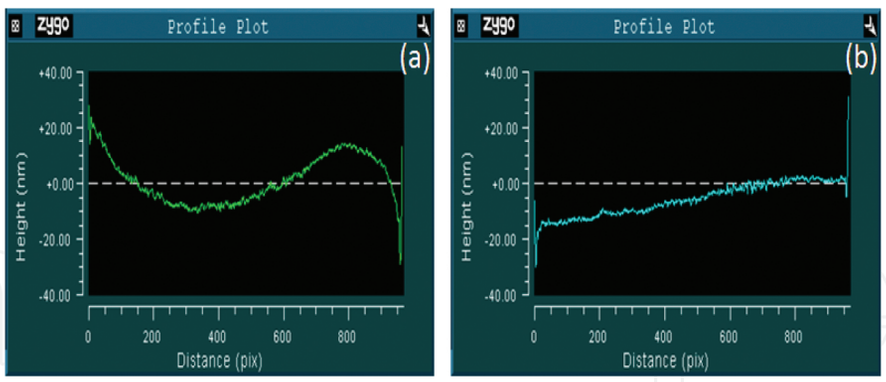

Figure 15. (a) 2-D surface height of **Figure 14c** along x-direction; and (b) along y-direction.

Another type of plano-concave surface of radius of curvature of 12744.1 mm at a focal length of −6000 mm has been tested using two-beam Zygo interferometer of type VeriFireMST and a wavelength of 632.467 nm. Circular fringes of the curved surface being tested are shown in **Figure 16(a)**; as shown from **Figure 16(a)**, the number of fringes/12 mm is around 15 fringes, which means the surface is nearly strong. The phase map of **Figure 16(a)** is shown in **Figure 16(b)**. Two-dimensional surface height of **Figure 16(b)** along X- and Y-directions is shown in **Figure 16(c)**.

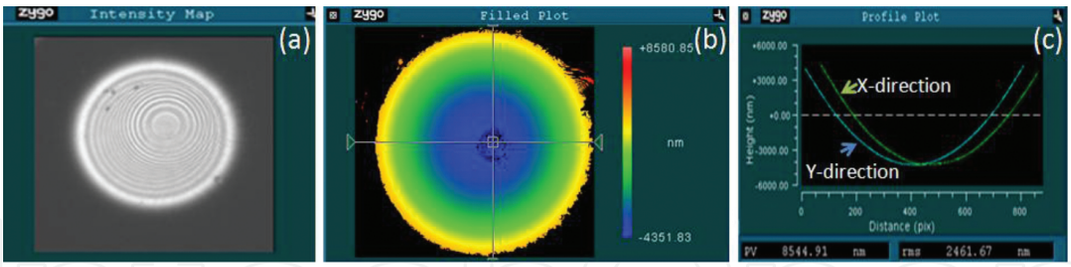

Figure 16. (a) Interferogram of the plano-concave surface; (b) phase map of (a); and (c) 2-D surface height of **Figure 16(b)** along *X*- and *Y*-directions.

3.2. Multiple-beam interferometry

Multiple beam fringes are extremely sharp. Simple measurements with such fringes can reveal surface micro-topography with a precession close to (λ/500). This advantage made multiple-beam interferometers so popular in revealing strongly curved surfaces and steep abrupt edges. Sharp fringes are obtained when the surfaces forming the cavity are coated with higher reflectivity film. The theory of the intensity distribution of Fabry-Perot fringes at reflection from an infinite number of beams collected was dealt with by [11]. Recently, Abdelsalam [12] modified an analytical equation correlate intensity distribution at reflection with a number of beams collected. It is found that 30 number of beams collected produce the same intensity profile as infinity number of beams are collected. In this section, we review multiple-beam Fizeau interferometry for thin film and curved strongly surfaces measurements.

3.2.1. Multiple-beam Fizeau interferometer for film thickness measurement

The schematic diagram of the Fizeau interferometer for film thickness measurement is illustrated in **Figure 17(a)**. Details of the measurement technique are explained by the author in [13]. The fringe pattern is digitized into the computer and then thinned to get the maximum or minimum of each individual fringe by a written program.

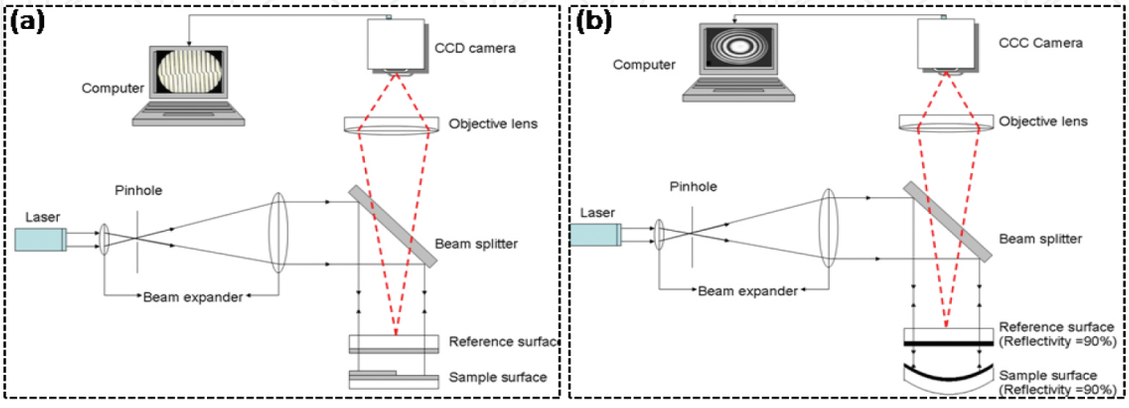

Figure 17. Schematic diagram of multiple-beam Fizeau interferometer for measurement of (a) film thickness and (b) curved surfaces.

Three different scan directions, *x*-scan, *y*-scan, and *x*-*y*-scan, were tested to obtain the best measurement. The program scans the image row by row for the *x*-scan, or by column in the *y*-scan, or in mixture for the *x*-*y*-scan. In **Figure 18(b)**, the *x*-scan, which scans row by row, was used. At each row, the program finds the pixel coordinate of the minimum intensity of that row. Selected fringes in the middle of **Figure 17(a)** were filtered and processed in the program until these fringes were thinned. The thinning of the selected fringes is shown in **Figure 18(b)**. The isometric plot shown in **Figure 18(c)** shows the average of the measured step height *h*. The average step height value of the film determined from at least 10 readings was 30.6 nm. It was found that the average step height value is very close to the nominal value (31 ± 3 nm).

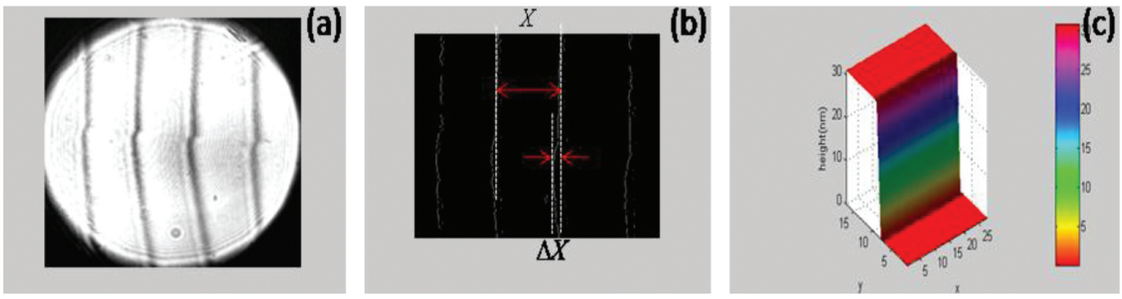

Figure 18. (a) Multiple-beam reflection fringes captured from Fizeau-Tolansky interferometer, (b) thinning of selected fringes in the middle of **Figure 2**, and (c) an isometric plot of (b).

3.2.2. Multiple-beam Fizeau interferometer for curved surfaces measurement

The schematic diagram of the Fizeau interferometer for curved surfaces measurement is illustrated in **Figure 17(b)**. Three curved surfaces of 25.4 mm in size and different radius of curvatures were coated with silver film of reflectivity nearly 90% and mounted parallel and close with the calibrated reference of nominally $\lambda/50$ flatness [7]. The reflectivity of the reference should be the same with the reflectivity of the object to obtain good contrast. **Table 1** shows types of curved surfaces being tested using **Figure 17(b)**.

Types of spherical smooth surfaces	Nominal value	Measured value
Large radius of curvature	$R \cong$ 38000.0 mm	$R \cong$ 37715.8 mm
Intermediate radius of curvature	$R \cong$ 18000.0 mm	$R \cong$ 17980.2 mm
Short radius of curvature	$R \cong$ 8000.0 mm	$R \cong$ 8314.7 mm

Table 1. The types of curved surfaces with nominal radius of curvatures and the measurement values by Zernike polynomial fitting method.

The three curved surfaces one by one were inserted in the interferometer and adjusted carefully until the inline interferogram is captured. **Figure 19(a–c)** shows the three inline interferograms of the corresponding three curved surfaces, large, intermediate, and short radius of curvatures,

respectively, after correction with flat fielding. The interferograms were reconstructed by Zernike polynomial fitting to extract the 3-D surface height as shown in **Figure 19(d–f)**. In Zernike polynomials fitting, the surface height function $Z_r(x_r, y_r)$ can be represented by a linear combination of M polynomials $F(x_r, y_r)$ and their weighting coefficients G [7]:

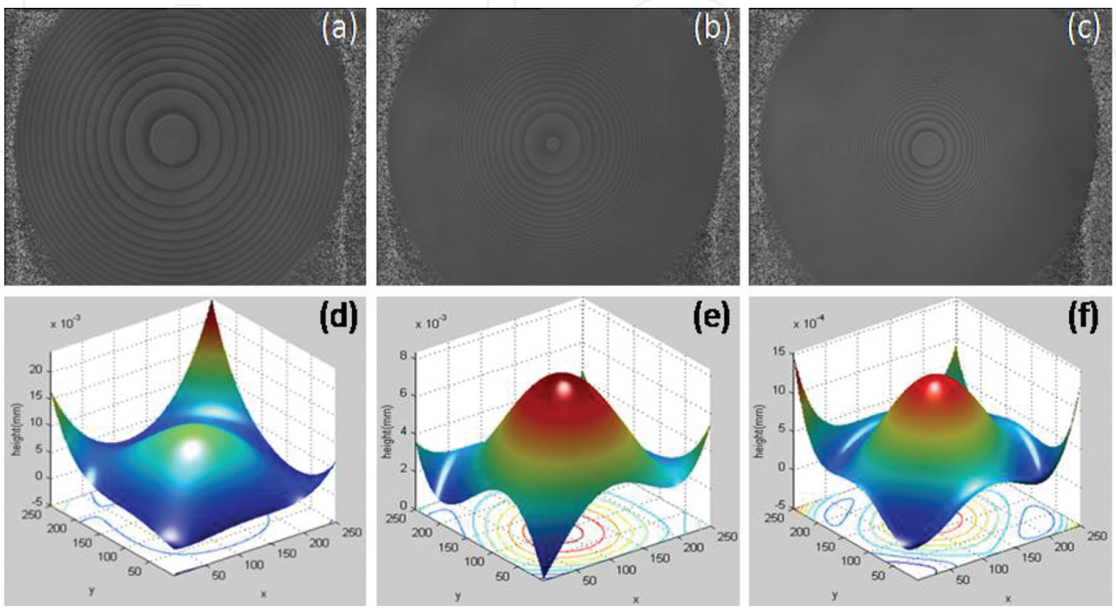

Figure 19. (a–c) captured interferograms after correction with flat fielding of the three curved surfaces, large, intermediate, and short radius of curvatures, (d–f) the corresponding 3-D surface height.

$$Z_r(x_r, y_r) = \sum_{j=1}^{M} F_j(x, y) G_j \tag{15}$$

where r is the sample index, so it is important to calculate the coefficients to represent the surface.

3.2.3. Testing parallelism degree on standard optical flat using Fizeau interferometer

Testing parallelism on standard optical flat of 25 mm in size using Fizeau interferometer is shown in **Figure 1(a)**. The optical flat is positioned on the front side as shown in **Figure 20(c)**, the left one. The interference pattern between the reference and the object is obtained and captured, as shown in **Figure 21(a)**, by color charge-coupled device (CCD) camera of frame rate of 15 fps, and pixel area of 2456 (y) × 2058 (x) μm^2 with a pixel size of 3.45 μm. The number of fringes of **Figure 21(a)** over 13 mm is found around 31 fringes or $\delta_1 = 31\lambda/2$. The optical flat is then positioned on the back side as shown in **Figure 20(c)**, the right one. The number of fringes of **Figure 21(b)** over 12 mm is found to be 32 fringes or $\delta_2 = 32\lambda/2$. The number of fringes can be accounted for manually or automatically by writing a small program.

http://dx.doi.org/10.5772/66275

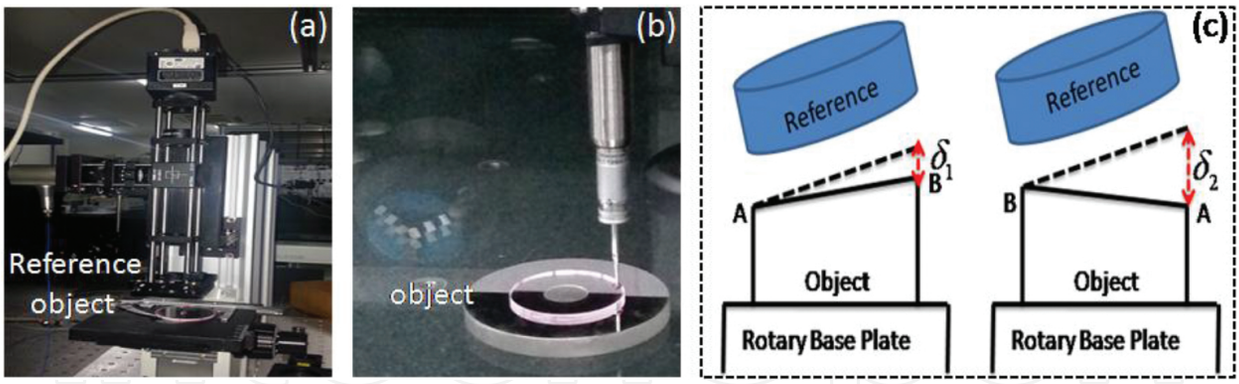

Figure 20. Testing parallelism degree on standard optical flats over 12 mm in length using (a) Fizeau interferometer and (b) coordinate measuring machine (CMM). Schematic diagram shows the locations of front and back surfaces of the sample in the interferometer (c).

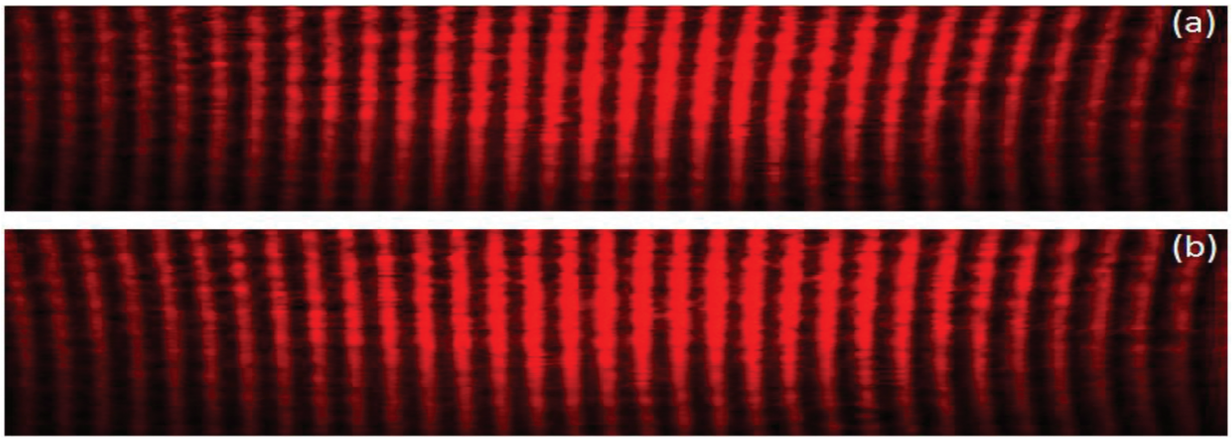

Figure 21. Fringe pattern produced at 12 mm on the (a) front side and (b) back side of the standard optical flat.

The change in the angular relationship is $\delta_2 - \delta_1 = 1\lambda/2$. But due to the rotation through 180°, there is a doubling effect. Therefore, the error in parallelism $=(\delta_2 - \delta_1)/2 = \lambda/4 \cong 160$ nm. The wavelength used in the experiment is a He-Ne laser of 632.8 nm, thus the optical flat has an error in parallelism of 160 nm over 12 mm at the middle of 25 mm.

The same size of front and back surfaces of the optical flat has been tested with coordinate measuring machine (CMM) with a suitable tip as shown in **Figure 20(b)** and the average difference between the two surface sides is calculated to be 200 nm.

3.3. Displacement interferometry

Displacement interferometry is usually based on the Michelson configuration or some variant of that basic design. Displacement measurement is defined simply a change in length. It is usually carried out by counting the number of fringes when either the object being measured or the reference surface is displaced. The fringes are counted by photodetectors and digital

electronics and the fraction is estimated by electronically sub-dividing the fringe [14, 15]. **Figure 22(a)** shows a configuration of homodyne interferometer. The homodyne interferometer uses a single frequency, f_1, laser beam. The beam from the reference is returned to the non-polarized beamsplitter (NPBS) with a frequency f_1, but the beam from the moving measurement path is returned with a Doppler-shifted frequency of $f_1 \pm \delta f$. These beams interfere in the NPBS and enter the photodetector. **Figure 22(b)** shows a heterodyne interferometer configuration. The output beam from a dual-frequency laser source contains two orthogonal polarizations, one with a frequency of f_1 and the other with a frequency of f_2 (separated by about 3 MHz using the Zeeman effect). A polarizing beamsplitter (PBS) reflects the light with frequency f_1 into the reference path. Light with frequency f_2 passes through the beamsplitter into the measurement path where it strikes the moving retro-reflector causing the frequency of the reflected beam to be Doppler shifted by $\pm\delta f$. This reflected beam is then combined with the reference light in the PBS and returned to a photodetector with a beat frequency of $f_2 - f_1 \pm \delta f$. This signal is mixed with the reference signal that continuously monitors the frequency difference, $f_2 - f_1$. With a typical reference beat of around 3 MHz, it is possible to monitor δf values up to 3 MHz before introducing ambiguities due to the beat crossing through zero. The displacement being measured for both homodyne and heterodyne is calculated from this equation $d = \lambda N/2$, where N is a fringe count and λ is the wavelength of the incident radiation. Homodyne interferometers have an advantage over heterodyne interferometers because the reference and measurement beams are split at the interferometer and not inside the laser.

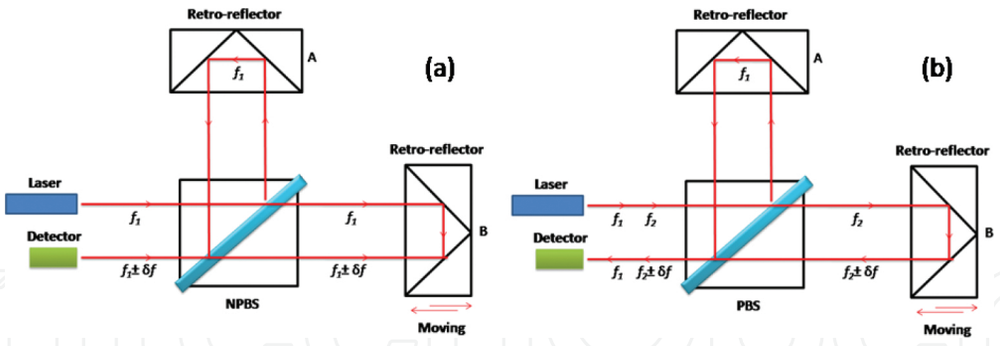

Figure 22. Homodyne interferometer configuration (a), and heterodyne interferometer configuration (b).

4. Fast phase-shifting interferometry

Phase shifting is an attractive and very robust technique for the analysis of fringe patterns. Since PS takes multiple images over a finite time period, it is sensitive to the time-dependent phase shifts due to vibrations. These vibrations are difficult to correct since the optimum algorithm depends on the frequency and the phase of the vibration. For a given vibration

http://dx.doi.org/10.5772/66275

amplitude, the phase error is a function of the ratio of the vibration frequency relative to the frame capture rate. Several methods have been used to try to get around the vibration problem in phase-shifting interferometry (PSI). One of those methods is speeding up the data collection process by capturing all frames simultaneously to be in single shot. Single-shot algorithm is reliable, fast, and less sensitive to vibration and turbulence in surface micro-topography measurement. In this section, we review one technique for fast phase-shifting-based single-shot parallel four step combined with Fizeau interferometer.

4.1. Single-shot parallel four-step phase-shifting Fizeau interferometer

In this section, the common path Fizeau interferometer is combined with a parallel four-step phase-shifting mechanism, thus real-time measurement is achieved [16]. By simultaneously capturing all four interferograms, this system is insensitive to vibration. The schematic diagram of the common path Fizeau interferometer combined with parallel four-step phase-shifting is shown in **Figure 23**. A helium-neon laser beam with vertical polarization passes through a collimating lens was expanded by the beam expander (BE). The collimated beam of the laser light falls upon the beamsplitter and are split into two copies. The transmitted copy from the beamsplitter is incident on the interferometer (the reference and the object) and then reflected from the interferometer with reference wave and object wave carrying the information of the tested curved surface. Note that the sample being tested was mounted as an object, and the quarter-wave plate of $\lambda/10$ flatness was mounted as a reference in the interferometer. The reflected reference and objects waves are introduced into another quarter-wave plate, whose fast axis is inclined at an angle of 45° relative to the polarization direction of the original reference wave. Thus, the object and reference waves are converted into the perpendicularly circularly polarized lights.

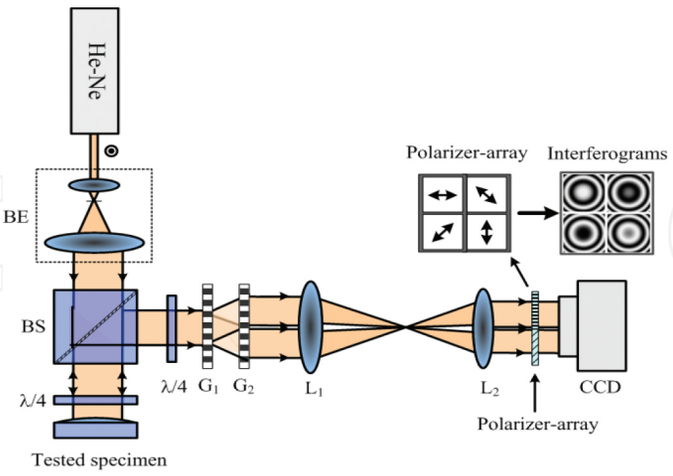

Figure 23. Configuration for single-shot parallel phase-shifting Fizeau interferometry, *BE*, beam expander; L_1-L_2, achromatic lenses with focal lengths $f_1 = 300$ mm, $f_2 = 150$ mm.

Two Ronchi phase gratings, G_1 and G_2, are located on the paths of the object and the reference waves. The axial distance between the two gratings is d, and their grating vectors are perpen-

dicular with each other. After passing through the gratings G_1 and G_2, both the object and the reference waves are diffracted into different orders. A polarizer array is mounted in front of the CCD camera to perform the polarization phase shifting. Thus, we can achieve the single-shot recording of the interferogram containing the information of the four phase-shifted interferograms whose phases of the reference (a quarter wave plate) wave are constant and the phases of the object were shifted. **Figure 24(a)** shows the four phase-shifted interferograms with $\pi/2$ rad generated from the proposed setup. Using the four-phase step algorithm [17], the phase distribution is wrapped between $-\pi$ and π due to arctangent function. The wrapped phase map is shown in **Figure 24(b)**. The wrapped phase map is then unwrapped [18] to remove the 2π ambiguity and the unwrapped phase map is shown in **Figure 24(c)**.

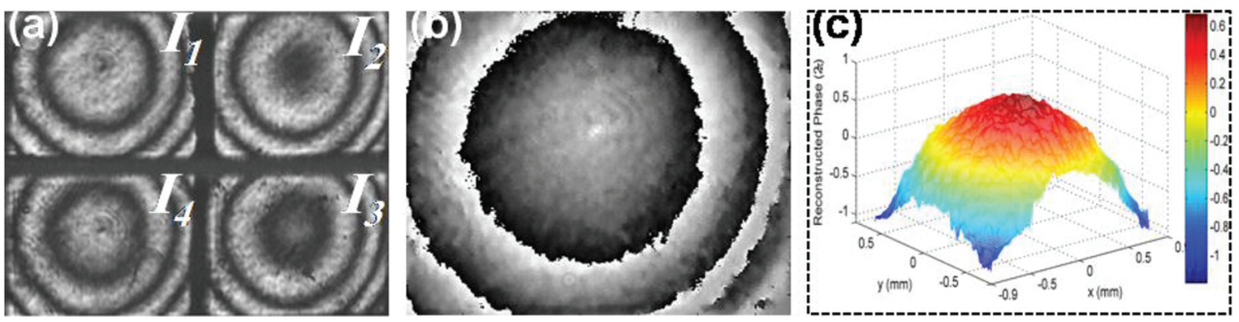

Figure 24. Experimental results of the single-shot, four-step phase-shifting using on-axis Fizeau interferometer; (a) intensity images of a spherical object with phase shift of 0, $\pi/2$, π, and $3\pi/2$; (b) wrapped phase map resulted from the four frames of (a); (c) 3-D unwrapped phase map of (b).

Another sample of step height has been tested using this technique. **Figure 25(a)** shows the four phase-shifted interferograms with $\pi/2$ rad generated from the proposed setup. The 3-D phase map is shown in **Figure 25(b)** and two-dimensional profile along the middle of **Figure 25(b)** is shown in **Figure 25(c)**. The step height has been measured again as shown in **Figure 23(c)** to confirm our method. As shown from **Figure 25(c)**, the proposed method is efficient, more robust, and highly accurate.

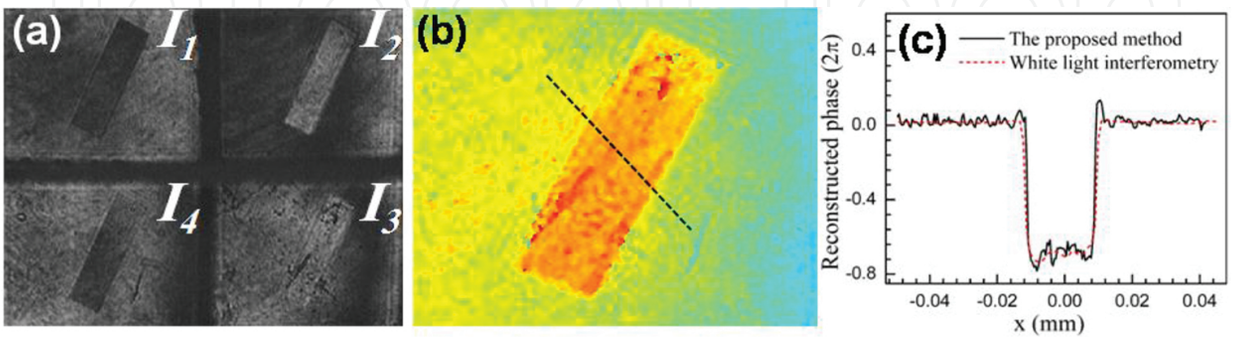

Figure 25. Experimental results of the single-shot, four-step phase-shifting using on-axis Fizeau interferometer; (a) intensity images of a step height object with phase shift of 0, $\pi/2$, π, and $3\pi/2$; (b) 3-D phase map of (a); (c) 2-D profile along the black line of (b).

5. Conclusion

In conclusion, we have presented new frontiers in interferometry carried out by the author for surface characterization. In this chapter, the fundamentals of interferometry and its ability to investigate the shape of surfaces with focus on denoising and impact of noise on phase unwrapping are presented. Also, limitations of optical instruments and optical aberrations measurement are discussed. Finally, we have described a fast phase-shifting technique, namely single-shot parallel four-step phase-shifting Fizeau interferometer for surface characterization. Experimental results are presented to verify the principles.

Author details

Dahi Ghareab Abdelsalam[1*] and Baoli Yao[2]

*Address all correspondence to: shosho_dahi@yahoo.com

1 Engineering and Surface Metrology Laboratory, National Institute for Standards, Egypt

2 State Key Laboratory of Transient Optics and Photonics, Xi'an Institute of Optics and Precision Mechanics, Chinese Academy of Sciences, Xi'an, China

References

[1] Greve, M.; & Sehm, K.: Direct determination of the numerical aperture correction factor of interference microscopes. Proceedings of the XI International Colloquium on Surfaces, Chemnitz, Germany, (2004), 156–163.

[2] Hecht, E.: Optics. Pearson Education, 5th edition. (2016).

[3] Wyant, J; & Creath, K.: Basic wavefront aberration theory for optical metrology. in Applied Optics and Optical Engineering. (1992); Vol. XI, R. R. Shannon and J. C. Wyant (eds.), Academic, New York, NY.

[4] Kemao, Q.: Two-dimensional windowed Fourier transform for fringe pattern analysis: principles, applications and implementations. Optics and Lasers in Engineering. (2007); 45, 304–317.

[5] Abdelsalam, D.; & Kim, D.: Coherent noise suppression in digital holography based on flat fielding with apodized apertures. Optics Express. (2011); 19, 17951–17959.

[6] Born, M.; Wolf, E.: Principles of Optics. Cambridge University Press. England (1980), 459–490.

[7] Abdelsalam, D.; Shaalan, M.; Eloker, M.; & Kim, D.: Radius of curvature measurement of spherical smooth surfaces by multiple-beam interferometry in reflection. Optics and Lasers in Engineering. (2010); 48, 643–649.

[8] Abdelsalam, D.; Baek, B & Kim, D.: Curvature measurement using phase shifting in-line interferometry, single shot off-axis geometry and Zernike's polynomial fitting. Optik-International Journal for Light and Electron Optics. (2012); 123, 422–427.

[9] Abdelsalam, D.; Min, J; Kim, D; & Yao, B.: Digital holographic shape measurement using Fizeau microscopy. Chinese Optics Letters. (2015); 13, 100701–1 to 100701–5

[10] Deck, L.L.: Fourier-Transform phase-shifting interferometry. Applied Optics. (2003); 42, 2354–2365.

[11] Holden, J.: Multiple-beam interferometer-intensity distribution in the reflected system. Proceedings of the Physical Society. (1949); 62, 405–417.

[12] Abdelsalam, D.: Numerical evaluation of the intensity distribution of a multiple-beam Fizeau fringe in reflection at finite number of beams collected. Optik- International Journal for Light and Electron Optics. (2012); 123, 422–427.

[13] Abdelsalam, D.; Baek, B; Abdel-Aziz, F; & Kim, D.: Highly accurate film thickness measurement based on automatic fringe analysis. Optik- International Journal for Light and Electron Optics. (2012); 123, 1444–1449.

[14] Birch, P.: Optical fringe sub-division with nanometric accuracy. Precision Engineering. (1990); 12, 195–198.

[15] Peggs, N; & Yacoot, A.: A review of recent work in sub-nanometre displacement measurement using optical and x-ray interferometry. Philosophical Transactions of the Royal Society of London A. (2002); 260, 953–968.

[16] Abdelsalam, D.; Yao, B.; Gao, P.; Min, J.; & Guo, R.: Single-shot parallel four-step phase shifting using on-axis Fizeau interferometry. Applied Optics. (2012); 51, 4891–4895.

[17] Kumar, U.; Bhaduri, B.; Kothiyal, M.; & Mohan Krishna.: Two wavelength micro-interferometry for 3-D surface profiling. Optics and Lasers in Engineering. (2009); 47, 223–229.

[18] Ghiglia, D.; & Pritt, M.: Two-Dimensional Phase Unwrapping: Theory, Algorithm, and Software, Wiley, New York, NY, USA (1998).